

# ADVANCED MATERIALS

## Supporting Information

for *Adv. Mater.*, DOI: 10.1002/adma.202108835

A High Conductivity 1D  $\pi$ -d Conjugated Metal–Organic Framework with Efficient Polysulfide Trapping-Diffusion-Catalysis in Lithium–Sulfur Batteries

*Dawei Yang, Zhifu Liang, Pengyi Tang, Chaoqi Zhang, Mingxue Tang, Qizhen Li, Jordi Jacas Biendicho, Junshan Li, Marc Heggen, Rafal E. Dunin-Borkowski, Ming Xu,\* Jordi Llorca, Jordi Arbiol,\* Joan Ramon Morante, Shu-Lei Chou,\* and Andreu Cabot\**

Copyright WILEY-VCH Verlag GmbH & Co. KGaA, 69469 Weinheim, Germany, 2018.

## Supporting Information

### **A High Conductivity One-Dimensional $\pi$ -d Conjugated Metal-Organic Framework with Efficient Polysulfide Trapping-Diffusion-Catalysis in Lithium-Sulfur Batteries**

*Dawei Yang+, Zhifu Liang+, Pengyi Tang+, Chaoqi Zhang, Mingxue Tang, Qizhen Li, Jordi Jacas Biendicho, Junshan Li, Marc Heggen, Rafal E. Dunin-Borkowski, Ming Xu\*, Jordi Llorca, Jordi Arbiol\*, Joan Ramon Morante, Shu-Lei Chou\*, Andreu Cabot\**

D. W. Yang, Z. F. Liang, C. Q. Zhang, Dr. J. J. Biendicho, Prof. J. R. Morante, Prof. A. Cabot  
Catalonia Institute for Energy Research - IREC,  
Sant Adrià de Besòs, Barcelona, 08930, Spain  
Email: [acabot@irec.cat](mailto:acabot@irec.cat)

D. W. Yang, C. Q. Zhang, Prof. J. R. Morante  
Department of Electronic and Biomedical Engineering  
Universitat de Barcelona, 08028 Barcelona, Spain

Z. F. Liang, Prof. J. Arbiol  
Catalan Institute of Nanoscience and Nanotechnology (ICN2)  
CSIC and BIST, Campus UAB, Bellaterra, 08193 Barcelona, Spain  
Email: [arbiol@icrea.cat](mailto:arbiol@icrea.cat)

Dr. P. Y Tang, Dr. M Heggen, Prof. R E. Dunin-Borkowski  
Ernst Ruska-Centre for Microscopy and Spectroscopy with Electrons and Peter Grünberg  
Institute Forschungszentrum Jülich GmbH 52425 Jülich, Germany

Dr. P. Y Tang  
State Key Laboratory of Information Functional Materials, 2020 X-Lab, ShangHai Institute of  
Microsystem and Information Technology, Chinese Academy of Sciences, Shanghai, P. R.  
China

Prof. M. X. Tang  
Center for High Pressure Science and Technology Advanced Research, Beijing 100094, China

Q. Z. Li  
Department of Biomedical Engineering, Southern University of Science and Technology  
(SUSTech), Shenzhen, Guangdong, 518055, China

Dr. J. S. Li

Institute of Advanced Study, Chengdu University, Chengdu 610106, China

Prof. J. Llorca

Institute of Energy Technologies, Department of Chemical Engineering and Barcelona Research Center in Multiscale Science and Engineering, Universitat Politècnica de Catalunya, EEBE, 08019, Barcelona, Spain

Prof. M. Xu

State Key Laboratory of Chemical Resource Engineering, Beijing University of Chemical Technology, Beijing 100029, P. R. China

Email: [mingxu@mail.buct.edu.cn](mailto:mingxu@mail.buct.edu.cn)

Prof. S. L. Chou

Institute for Carbon Neutralization, College of Chemistry and Materials Engineering, Wenzhou University, Wenzhou, Zhejiang 325035, China

E-mail: [chou@wzu.edu.cn](mailto:chou@wzu.edu.cn)

Prof. J. Arbiol, Prof. A. Cabot

ICREA

Pg. Lluís Companys 23, 08010 Barcelona, Spain

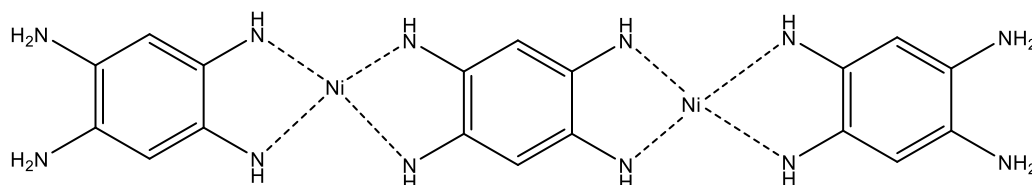
+ These authors contributed equally to this work

## Experimental Procedures

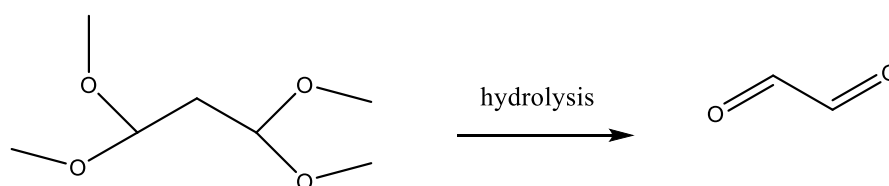
*Chemicals:* 1,3-dioxolane (DOL, 99.5%), lithium nitrate ( $\text{LiNO}_3$ , 99.98%), lithium sulfide ( $\text{Li}_2\text{S}$ , 99.9%), poly(vinylidene fluoride) (PVDF, 99%), and Super P (99%) were purchased from Alfa Aesar. 1,2,4,5-benzenetetramine tetrahydrochloride ( $\geq 96\%$ ), 1,1,3,3-tetramethoxypropane (99%), nickel acetate tetrahydrate (99.99%), triethylamine ( $\text{Et}_3\text{N}$ , 99.5%), N-methyl-2-pyrrolidone (NMP, 99.99%), sublimed sulfur (99.98%), and carbon disulfide ( $\text{CS}_2$ , 99.9%) were purchased from Sigma-Aldrich. Lithium bis(trifluoromethanesulfonyl) imide ( $\text{LiTFSI}$ , 99%) was purchased from Acros Organics and 1,2-dimethoxymethane (DME, 99%) was from Honeywell. All chemicals were used without further purification.

*Synthesis of Ni-MOF-1D:* The synthesis of Ni-MOF-1D is based on the following steps [6]: First,  $\text{Ni}^{2+}$  ions are coordinated with two 1,2,4,5-benzenetetramine. Then, the 1,1,3,3-tetramethoxypropane is hydrolyzed to malondialdehyde. Finally, the malondialdehyde is used as linker to react with the two 1,2,4,5-benzenetetramine:

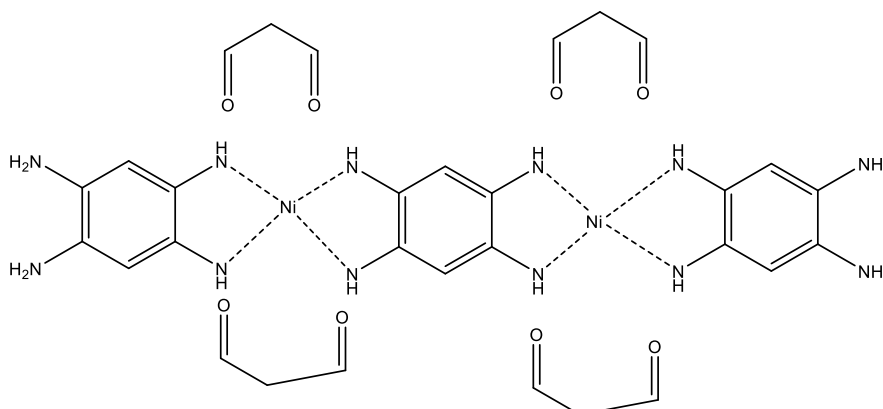
First,



Then,



and finally,



More in detail, 1,2,4,5-benzenetetramine tetrahydrochloride (284 mg, 1 mol), 1,1,3,3-tetramethoxypropane (165  $\mu\text{L}$ , 2 mol) and nickel acetate tetrahydrate (248.8 mg, 1 mol) were placed into a 25 mL three-neck flask. Subsequently, 15 mL of water was added. Then the mixture was stirred for half an hour. Then  $\text{Et}_3\text{N}$  (0.55  $\mu\text{L}$ , 4 mol) was added to the above mixture, which was then heated at 100  $^\circ\text{C}$  for 24 h with stirring. The obtained precipitate was filtrated by vacuum and then washed with water and a small amount of methanol. The material was vacuum dried for 12 h under 60  $^\circ\text{C}$ .

*Synthesis of S@Ni-MOF-1D and S@Super P:* Typically, Ni-MOF-1D and sulfur powder were well mixed with a weight ratio of 1:3, and then heated at 155  $^\circ\text{C}$  for 8 h under Ar protection in a sealed glass bottle. Then the redundant sulfur not incorporated into Ni-MOF-1D was washed by 10 mL  $\text{CS}_2$  and ethanol solution (1:4, volume ratio) for several times. For comparison, S@Super P was also prepared by the same method.

**Materials Characterization:** X-ray diffraction (XRD) patterns were detected using a Bruker AXS D8 Advance X-ray diffractometer with Cu K radiation ( $\lambda = 1.5106 \text{ \AA}$ ) operating at 40 kV and 40 mA. The morphology, structure and composition of the samples were characterized by field emission scanning electron microscopy (FE-SEM, ZEISS Auriga) equipped with an energy dispersive X-ray spectroscopy (EDX). High-resolution TEM (HRTEM) studies were carried out using a FEI Tecnai F20 microscope at 200 kV. High angle annular dark-field scanning transmission electron microscopy (HAADF-STEM) images and elemental mapping were obtained in a spherical aberration-corrected transmission electron microscope FEI Titan 80-300 at 300 kV and FEI Titan G2 80-200 ChemiSTEM with four EDX detectors and operated at 200 kV. The Integrated differential phase-contrast STEM (iDPC-STEM) images were obtained under a spherical aberration (Cs)-corrected STEM (FEI Titan Cubed Themis G2 300) operated at 300 kV. X-ray photoelectron spectroscopy (XPS) measurements were conducted by operating at 150 W and a Phoibos 150 MCD-9 detector. X-ray absorption near-edge structure (XANES) and extended X-ray absorption fine structure (FT-EXAFS) were performed at the Beijing Synchrotron Radiation Facility (BSRF). XAFS data were analyzed according to the standard procedures using ATHENA program. The content of sulfur within the cathode composites was estimated by thermogravimetric (TGA) on a PerkinElmer Diamond TG/DTA instrument under nitrogen ( $\text{N}_2$ ) at a heating rate of 10  $^\circ\text{C min}^{-1}$ . UV-vis absorption spectrum

was tested using PerkinElmer Lambda 950 UV–vis spectrophotometer. Nitrogen adsorption-desorption isotherms were recorded to calculate the specific surface area and analysis of the pore size distribution by Brunauer-Emmett-Teller method on a Tristar II 3020 Micromeritics system. The well-resolved solid-state Magic Angle Spinning Nuclear Magnetic Resonance (MAS-NMR) spectra were acquired on a Bruker 400 MHz spectrometer with 4.0 mm HX double resonance probe at the  $^1\text{H}$  and  $^{13}\text{C}$  Larmor frequencies of 400.17 and 100.62 MHz, respectively. Continuous-wave electron paramagnetic resonance (CW-EPR) spectrum was acquired on a Bruker EMXmicro spectrometer at X-band (9.5 GHz).

*Li-S Cell Assembly and Measurements:* S@host composites (S@Ni-MOF-1D, and S@Super P), PVDF binders and Super P (weight ratio =8:1:1) were dispersed in NMP. The obtained slurry was coated on an aluminum foil and vacuum dried at 60 °C overnight. The coated aluminum foil was then punched into small disks with diameter of 12 mm. Sulfur loading was around 1.0-1.2 mg cm<sup>-2</sup>. CR2032 coin-type cells were assembled in an Ar-filled glove box with lithium foils as counter electrodes, Celgard 2400 membranes as separators, and 1.0 M LiTFSI in DOL/DME solvent (1:1 vol%) with 0.2 M LiNO<sub>3</sub> additive as the electrolyte. The electrolyte/sulfur ratio was controlled to be about 20 μL mg<sup>-1</sup> for the common coin cells. The galvanostatic charge/discharge (GCD) measurements were conducted at a voltage window of 1.7-2.8 V vs. Li<sup>+</sup>/Li on a Neware BTS4008 battery tester with different C rates. The battery tester BCS-810 from Bio Logic was used to carry out the cyclic voltammetry (CV) measurements at a scan rate of 0.1-0.5 mV s<sup>-1</sup>, and the electrochemical impedance spectroscopy (EIS) tests with a voltage amplitude of 10 mV in the frequency range 0.01-10<sup>5</sup> Hz.

*Synthesis of Li<sub>2</sub>S<sub>4</sub> solutions for adsorption test:* Sulfur and Li<sub>2</sub>S with a molar ratio of 3:1 dissolved in an appropriate amount of DME/DOL (volume ratio of 1:1) solution under continuous stirring overnight, eventually obtaining a homogeneous dark brown solution. To evaluate the absorption ability for polysulfide, 15 mg of S@Ni-MOF-1D and S@Super P were added to 3.0 mL 10 × 10<sup>-3</sup> M Li<sub>2</sub>S<sub>4</sub> solution under Ar atmosphere, respectively.

*Symmetric Cell Assembly and Measurements:* Electrodes for symmetric cells were prepared by using the same process as that for LSBs. Two pieces of the same electrode (average loading about 0.5 mg cm<sup>-2</sup>) were used as working and counter electrodes with 40 μL of electrolyte containing 0.5 mol L<sup>-1</sup> Li<sub>2</sub>S<sub>6</sub> and 1 mol L<sup>-1</sup> LiTFSI dissolved in DOL/DME (v/v = 1/1). For

comparison, symmetric cells with electrolyte 1 mol L<sup>-1</sup> LiTFSI dissolved in DOL/DME (v/v = 1/1) were also assembled and tested under CR2032 coin cells. The CV measurements for all the symmetric cells were performed at a scan rate of 20 mV s<sup>-1</sup> in a voltage window between -1.0 and 1.0 V.

*Measurement of Nucleation of Li<sub>2</sub>S*: Nucleation and dissolution of Li<sub>2</sub>S were tested in 2032 coin cells to investigate the liquid-solid reaction kinetics. A certain amount of host materials loaded on the carbon papers applied as work electrode. Li foil worked as the counter electrode. The catholyte consisted of 20 μL of 0.25 M Li<sub>2</sub>S<sub>8</sub> and 1.0 M LiTFSI in tetraethylene glycol dimethyl ether solution. In the case of anolyte, it contained 20 μL of a 1.0 M LiTFSI solution without Li<sub>2</sub>S<sub>8</sub>. The cells were first discharged at a current of 0.112 mA to 2.19 V and then hold the voltage at 2.05 V until the current decreased to 10<sup>-2</sup> mA for Li<sub>2</sub>S nucleation and growth.

### DFT calculations

Density functional theory (DFT) calculations were performed to understand the interactions of LiPS species with Ni-MOF-1D cathode hosts. Spin-polarized DFT calculations were performed in the VASP code using projector augmented wave (PAW) pseudopotentials.<sup>[1,2]</sup> The SCAN meta-GGA functional was used in this system for obtaining the accurate absorbing configurations and energy as it takes up to 17 interaction force in to consideration between atoms,<sup>[3,4]</sup> which provides an accurate description of short, intermediate and long-range van der Waals interactions.<sup>[5]</sup>

Ni-MOF-1D was built with a vacuum layer with the Z-axis by 0.15 nm and the Y-axis by 15 nm. The free energy stage for each absorbent was calculated by following equation, taking \*-Li<sub>2</sub>S<sub>2</sub> → \*-Li<sub>2</sub>S<sub>4</sub>:

$$E_{\text{free*-Li}_2\text{S}_2 \rightarrow \text{*Li}_2\text{S}_4} = E_{\text{free*-Li}_2\text{S}_4} - E_{\text{free*-Li}_2\text{S}_2} - 2 \cdot \frac{1}{8} \cdot E_{\text{freeS}_8}$$

where,  $E_{\text{free*-Li}_2\text{S}_2 \rightarrow \text{*Li}_2\text{S}_4}$  is the free energy variation for the reaction of \*-Li<sub>2</sub>S<sub>2</sub> → \*-Li<sub>2</sub>S<sub>4</sub>, the  $E_{\text{free*-Li}_2\text{S}_4}$ , the  $E_{\text{free*-Li}_2\text{S}_2}$  and the  $E_{\text{freeS}_8}$ , are the absolute DFT obtained energy after considering ZPE, TS correction. In terms of the energy of Li ions, it was taken the 1/4 Li bulk (primitive cell with 4 Li atoms). Band structure was calculated with HSE06 functional accuracy.

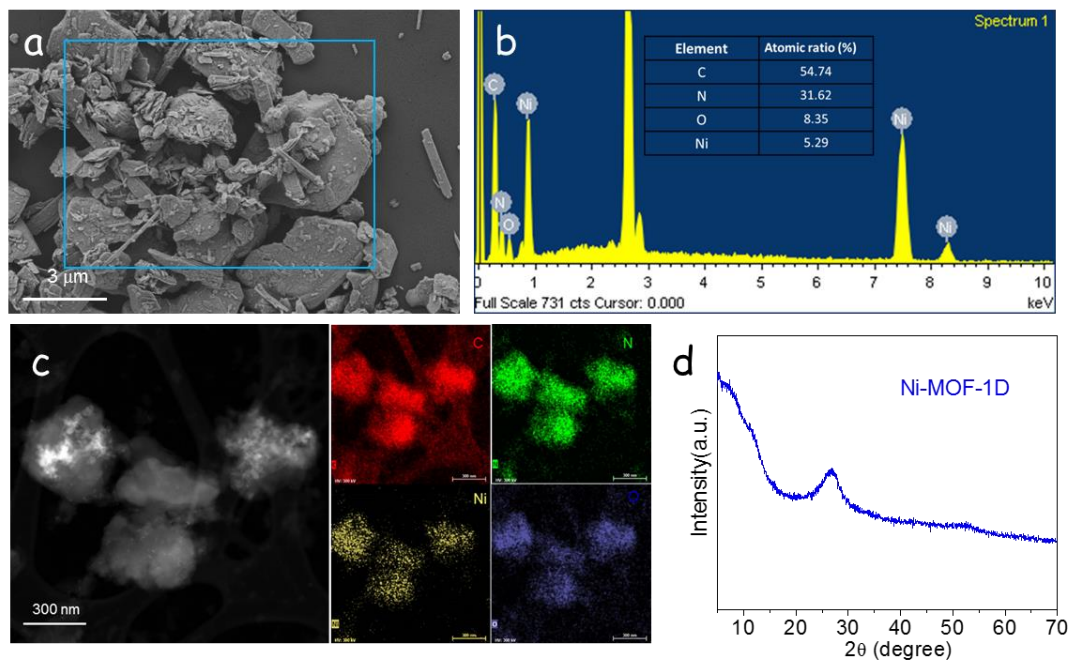


**Figure S1.** (a,b) SEM image and EDX spectrum of Ni-MOF-1D sample. (c) High magnification STEM-HAADF image and EDX elemental mapping showing the elemental distribution in a Ni-MOF-1D sample. (d) XRD pattern of Ni-MOF-1D.

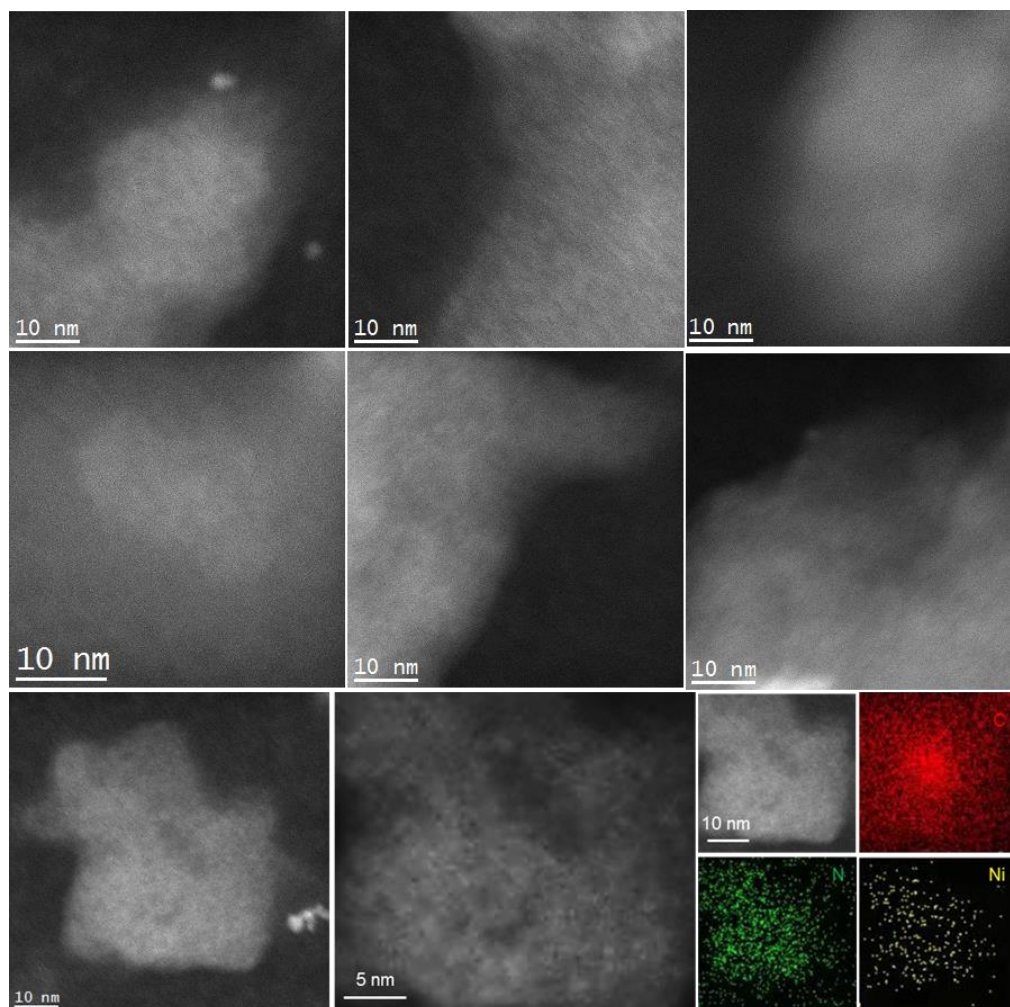


**Figure S2.** High magnification HAADF-STEM images and detailed STEM-EDX elemental maps of a Ni-MOF-1D catalyst.

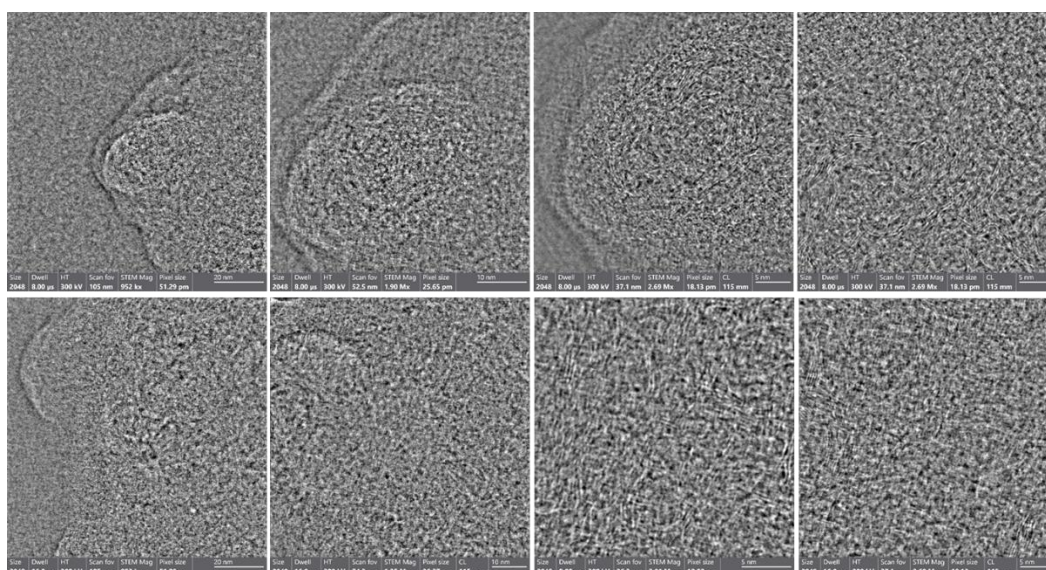


**Figure S3.** iDPC-STEM images of Ni-MOF-1D with different magnifications.

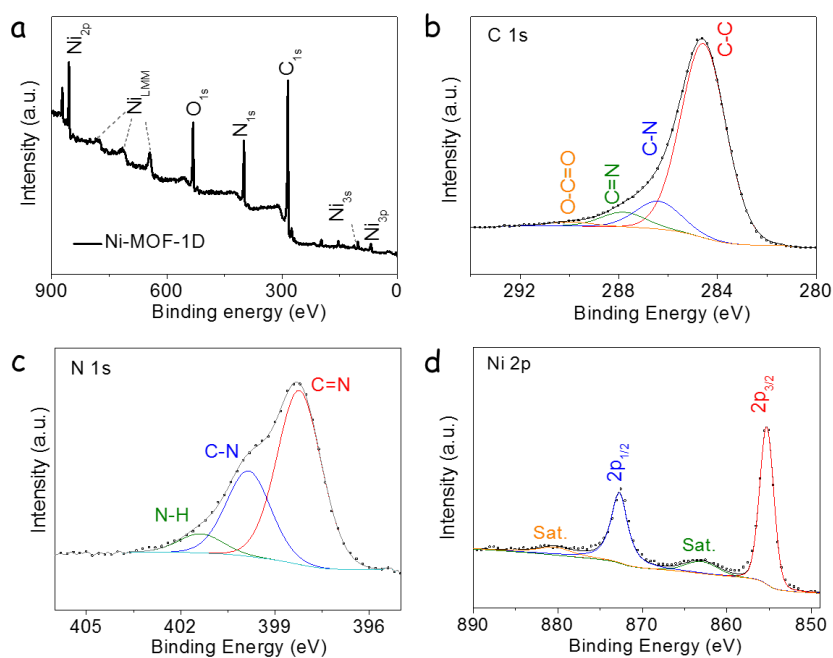
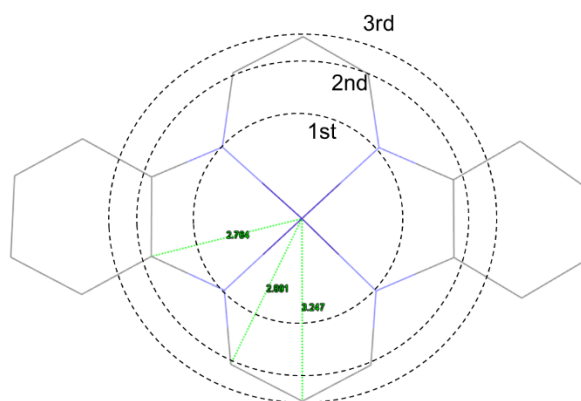


**Figure S4.** (a) XPS survey spectrum of Ni-MOF-1D. (b-d) High resolution XPS spectra of b) C 1s, c) N 1s, and d) Ni 2p.

**Table S1** Detailed EXAFS fitting model and parameters of Ni-MOF-1D.



	N	$R / \text{\AA}$	$\sigma$	$\Delta E / \text{eV}$
N (1st)	4	1.86	0.002	-8.37
C (2nd)	8	2.73	0.012	-8.37
C (3rd)	2	3.08	0.035	-8.37

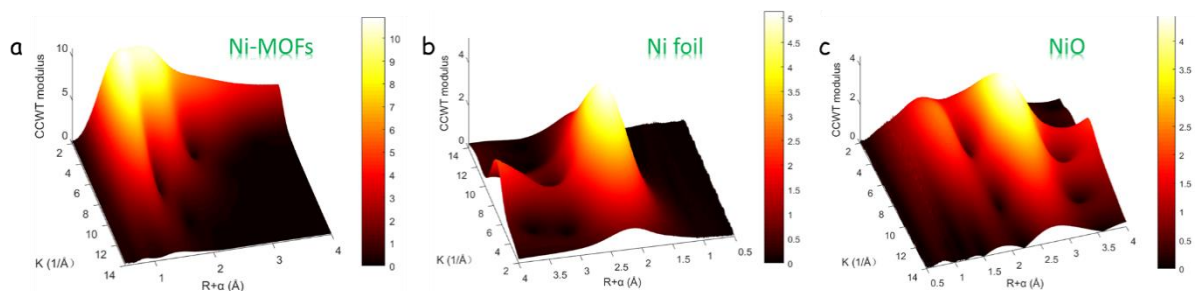


**Figure S5.** Wavelet transform (WT) analysis of (a) Ni-MOF-1D, (b) Ni foil, and (c) NiO.

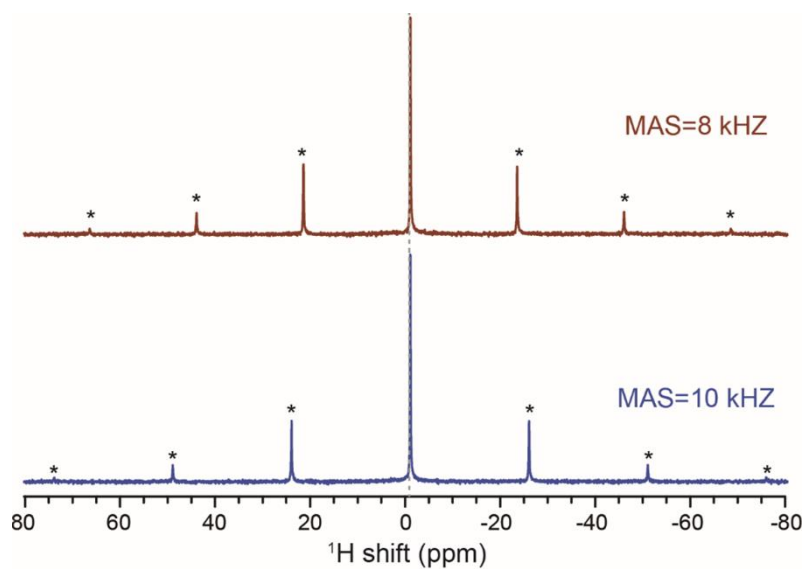


**Figure S6.**  $^1\text{H}$  NMR spectra of the obtained sample of Ni-MOF-1D.

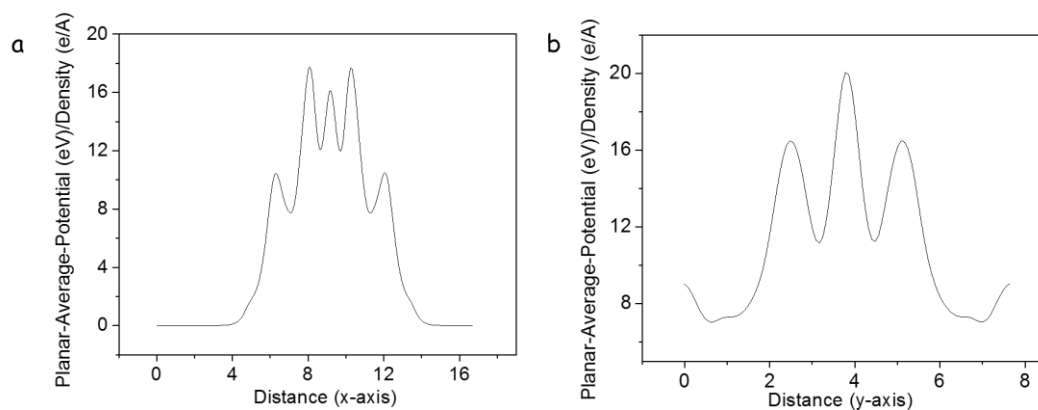


**Figure S7.** (a) Projected integral of the charge density in the non-periodic direction. (b) Projected integral of the charge density in the periodic direction of Ni-MOF-1D.

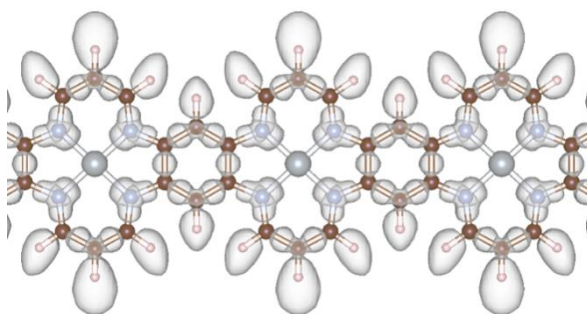


**Figure S8.** Calculated electron localization function (ELF) of Ni-MOF-1D.

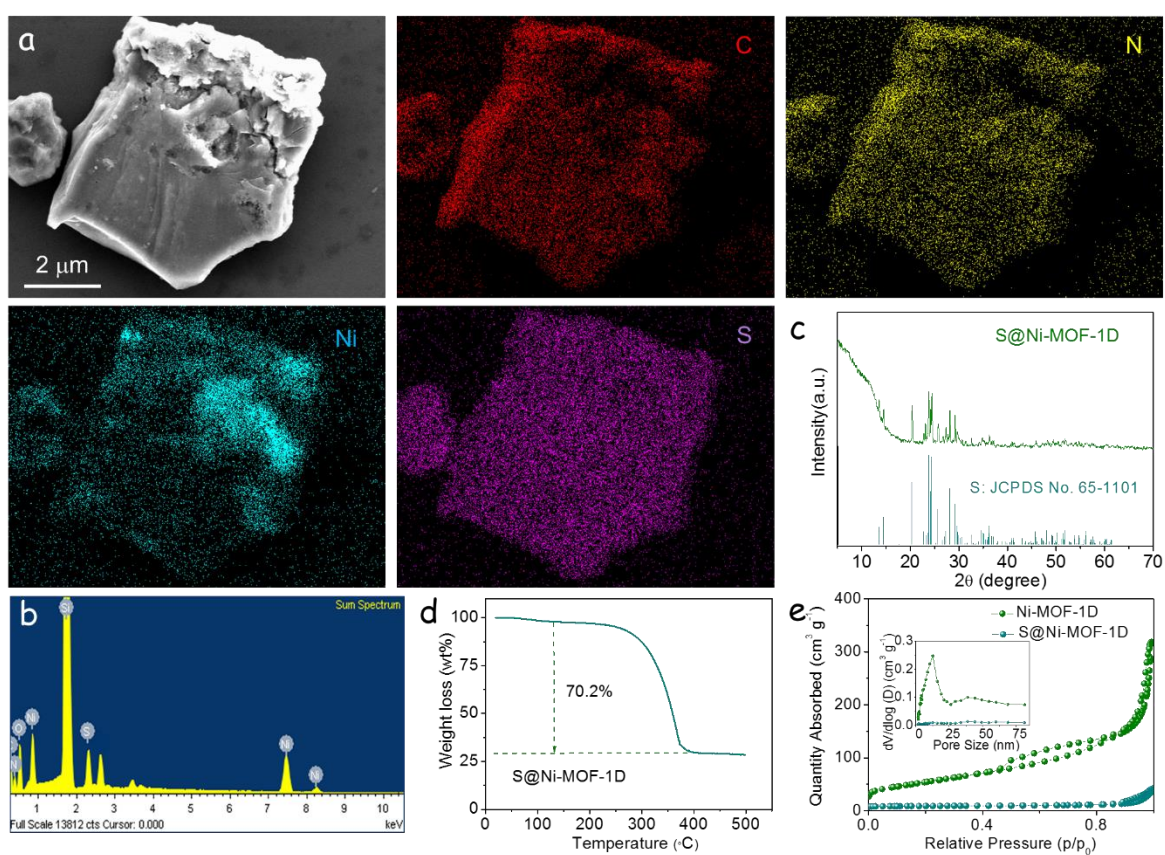


**Figure S9.** (a) SEM-EDX compositional maps and (b) EDX spectra of S@Ni-MOF-1D. (c) XRD pattern of S@Ni-MOF-1D. (d) TGA profile from S@Ni-MOF-1D measured in N<sub>2</sub> atmosphere. (e) N<sub>2</sub> adsorption-desorption isotherms of Ni-MOF-1D and S@Ni-MOF-1D. Inset: Pore size distribution of Ni-MOF-1D and S@Ni-MOF-1D.

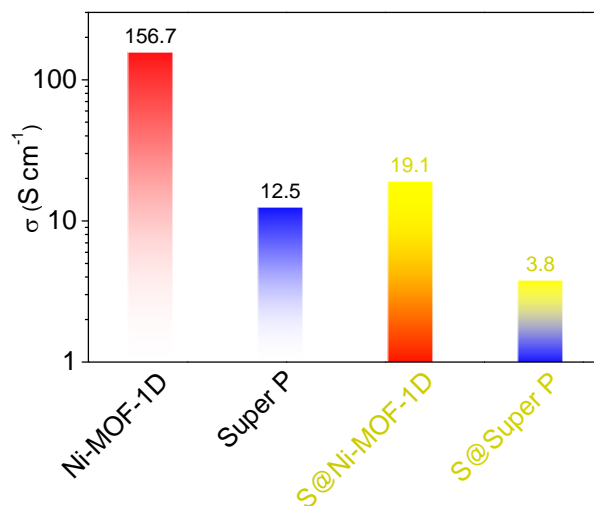


**Figure S10.** Electrical conductivity of the two hosts tested before and after fusion with sulfur.

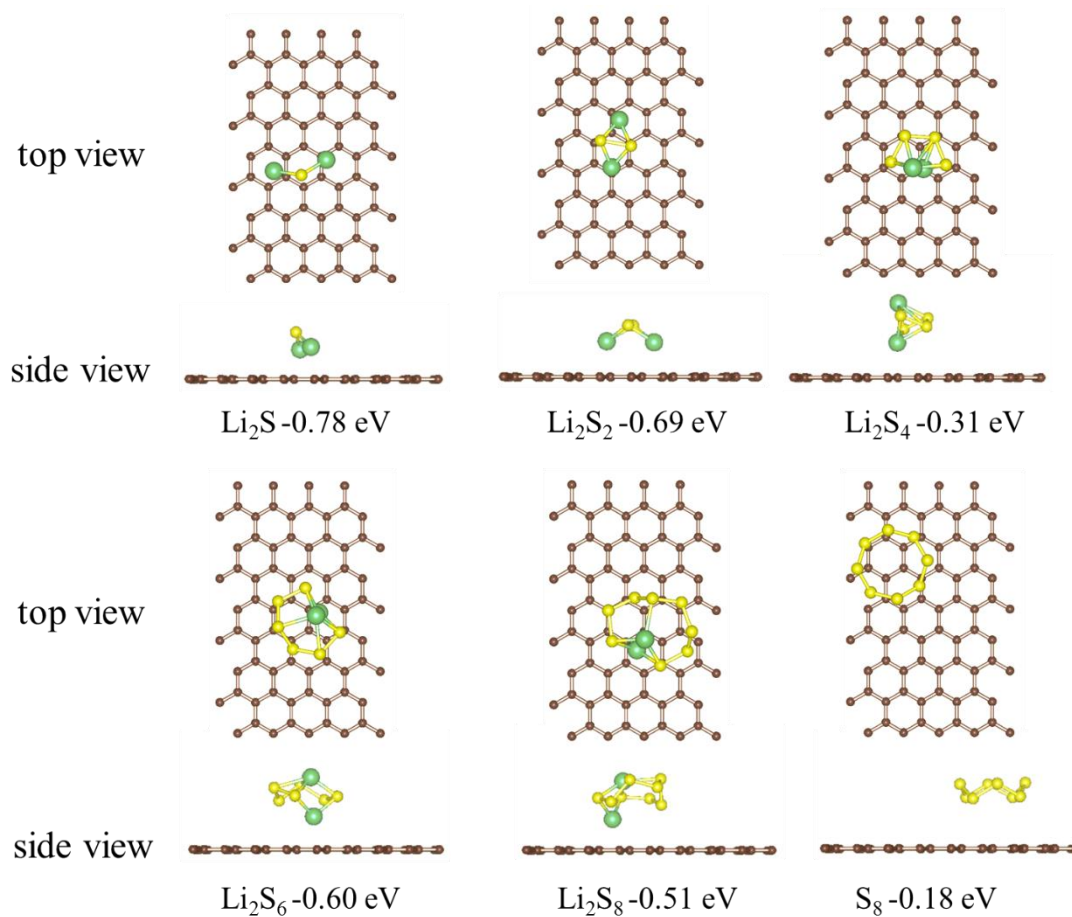


**Figure S11.** Binding energies and adsorbed structures of LiPS on the surface of carbon calculated by DFT.

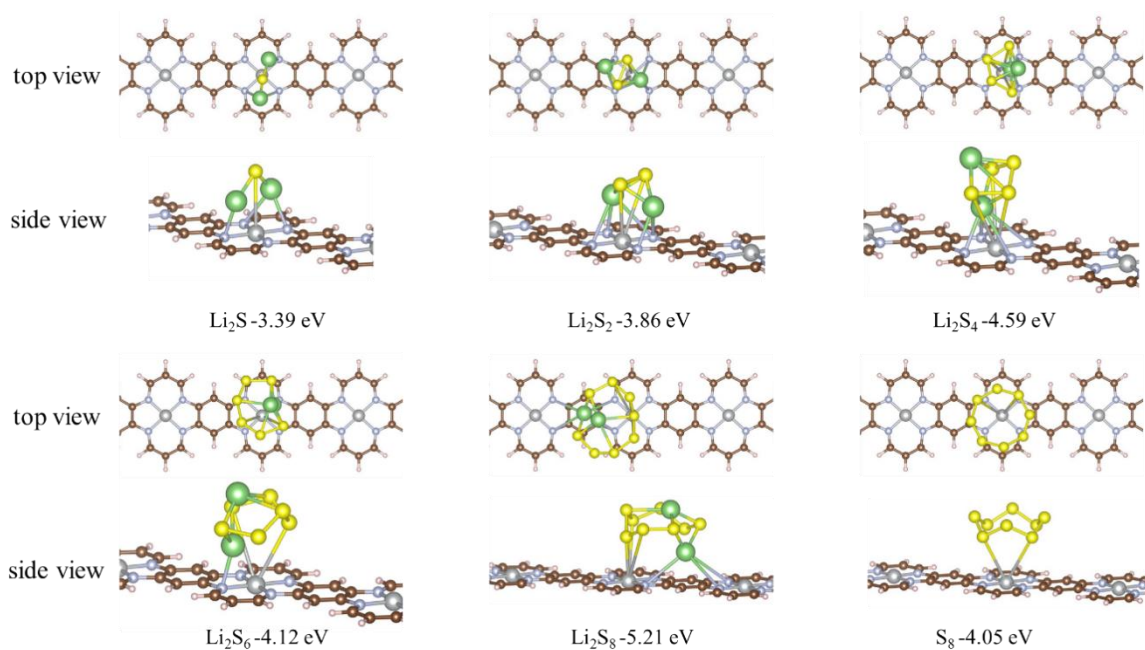


**Figure S12.** Binding energies and adsorbed structures of LiPS on the surface of Ni-MOF-1D calculated by DFT.

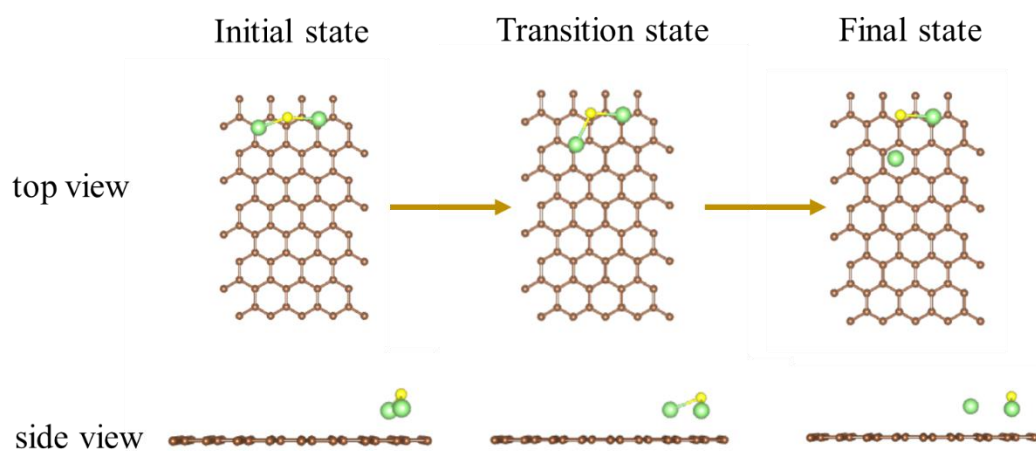


**Figure S13.** The optimized adsorption configuration of  $\text{Li}_2\text{S}$  decomposition on carbon.

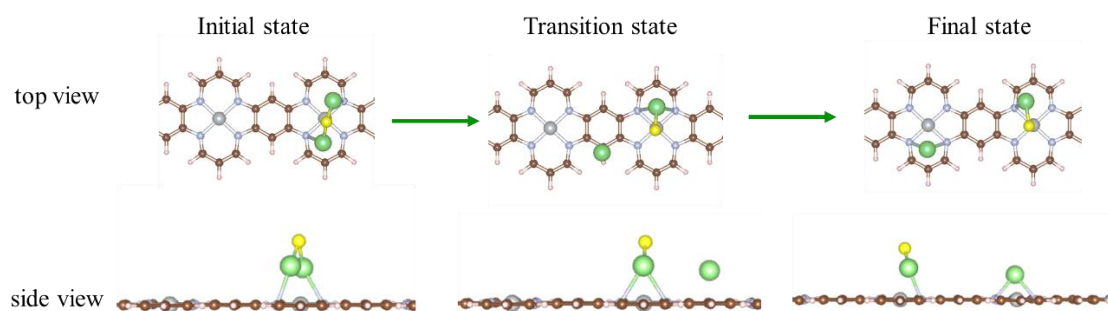


**Figure S14.** The optimized adsorption configuration of  $\text{Li}_2\text{S}$  decomposition on Ni-MOF-1D.

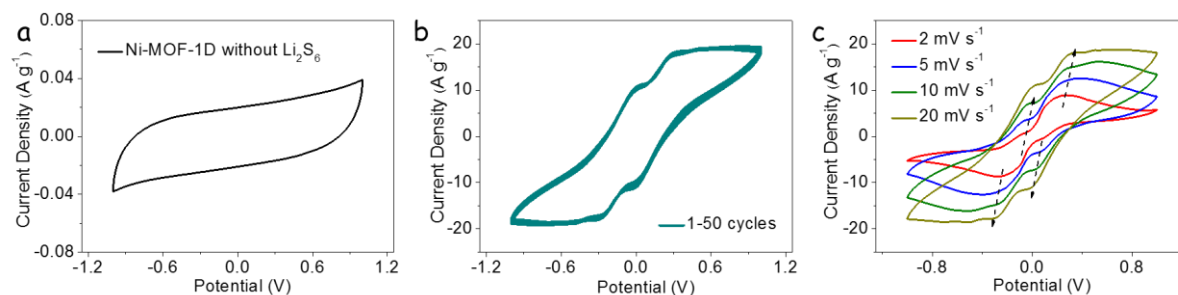


**Figure S15.** (a) CV curve of Ni-MOF-1D as electrode measured in symmetric coin cell configuration using an electrolyte containing  $1 \text{ mol L}^{-1}$  LiTFSI dissolved in DOL/DME ( $v/v = 1/1$ ). (b) CV curves of symmetric cells from 1 to 50 cycles. (c) CV profiles of Ni-MOF-1D electrodes in symmetric cells at scan rate from  $2 \text{ mV s}^{-1}$  to  $20 \text{ mV s}^{-1}$ .

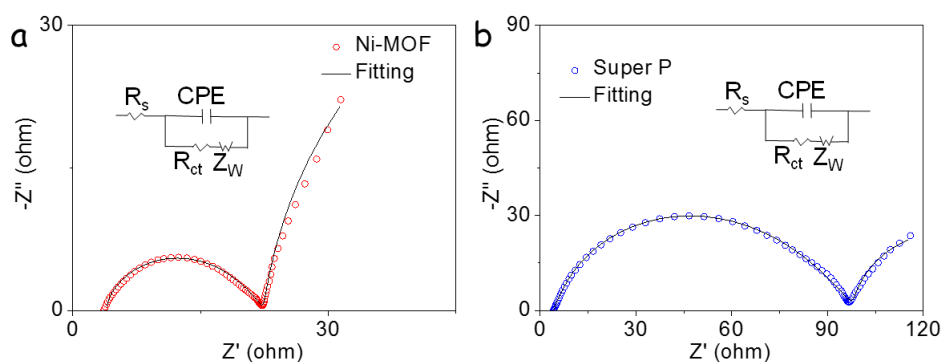


**Figure S16.** EIS spectra of symmetrical cells with different host materials, Ni-MOF-1D (a) and Super P (b), using an electrolyte containing  $0.5 \text{ mol L}^{-1}$   $\text{Li}_2\text{S}_6$  and  $1 \text{ mol L}^{-1}$  LiTFSI dissolved in DOL/DME ( $v/v = 1/1$ ).

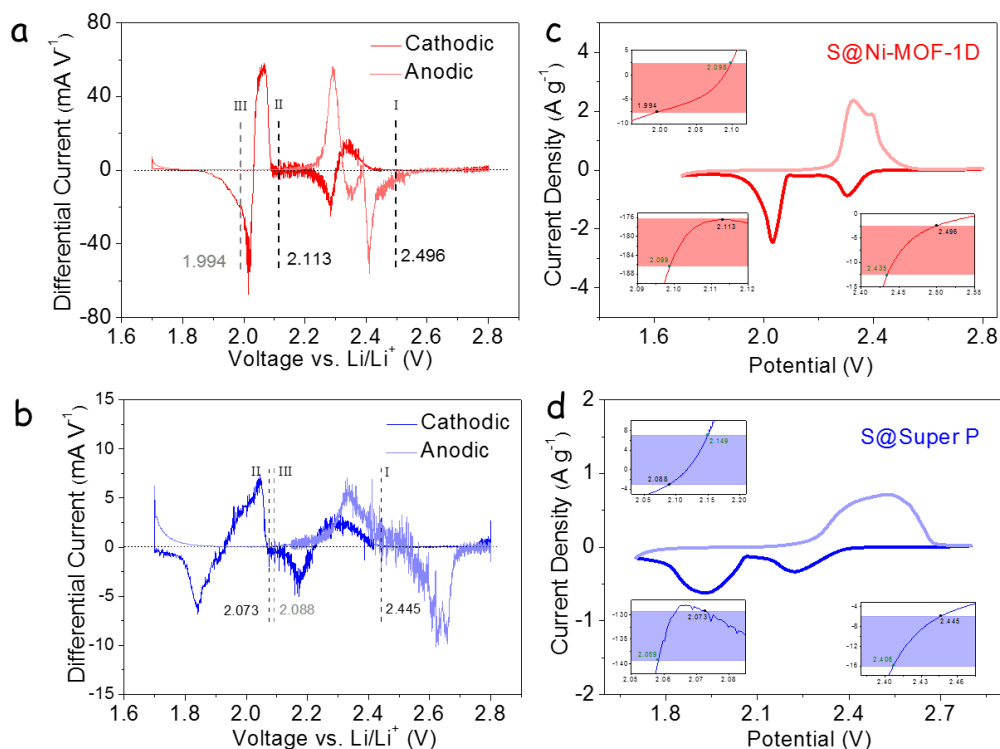


**Figure S17.** Onset potential for Li-S redox reactions. (a,b) Differential CV curves of S@Ni-MOF-1D (a) and S@Super P (b). The baseline voltage and current density are defined as the value before the redox peak, where the variation on current density is the smallest, namely  $dI/dV = 0$ . Baseline voltages are denoted in black for cathodic peak I, II, and in gray for anodic peak III, respectively. (c,d) CV curves and corresponding onset potentials of redox peak I, II, and III (inset): (c) S@Ni-MOF-1D, (d) S@Super P. Following a common definition employed in electrocatalysis, the onset potential is determined when the current density is  $10 \mu\text{A cm}^{-2}$  beyond the corresponding baseline current density (more specifically,  $10 \mu\text{A cm}^{-2}$  more negative than baseline current density for cathodic peaks or  $10 \mu\text{A cm}^{-2}$  positive than baseline current density for anodic peaks). As shown in the inset of c and d, the baseline voltages are the same as in a and b, while the colored region indicates the gap in current density ( $10 \mu\text{A cm}^{-2}$ ).

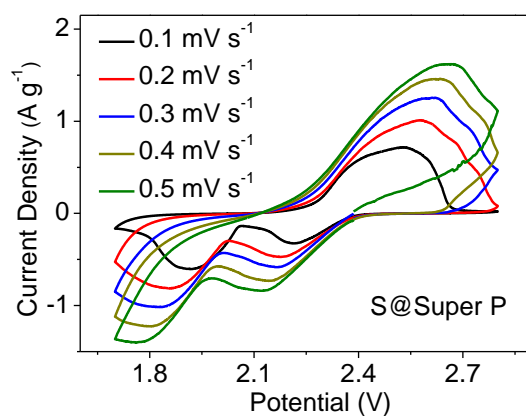


**Figure S18.** CV curves of S@Super P at different scan rates.

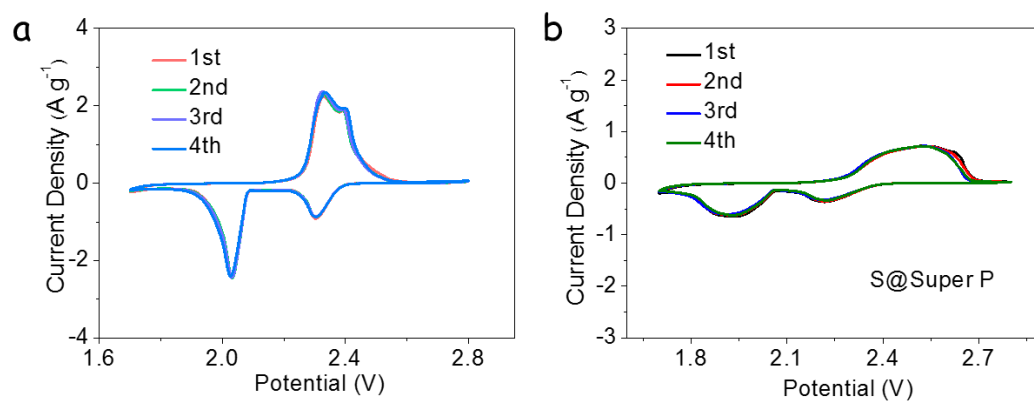


**Figure S19.** First four cycles of CV curves of (a) S@Ni-MOF-1D, and (b) S@Super P performed at a scan rate of 0.1 mV s<sup>-1</sup>.

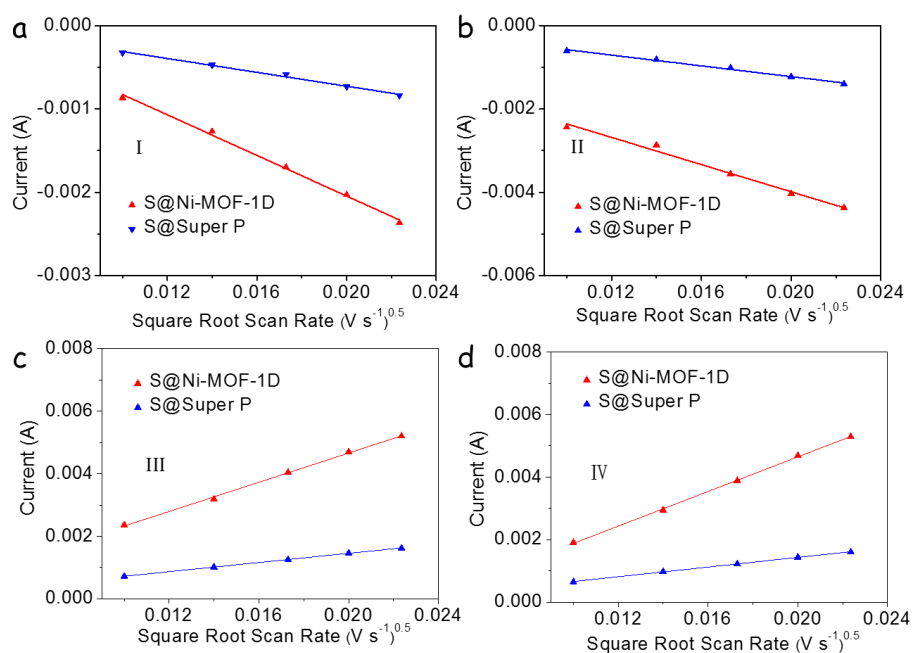


**Figure S20.** Plots of CV peak current for (a) the first cathodic reduction process (I:  $S_8 \rightarrow Li_2S_4$ ), (b) the second cathodic reduction process (II:  $Li_2S_4 \rightarrow Li_2S_2/Li_2S$ ), (c) the first anodic oxidation process (III:  $Li_2S_2/Li_2S \rightarrow Li_2S_4$ ), and (d) the second anodic oxidation process (IV:  $Li_2S_4 \rightarrow S_8$ ) versus the square root of the scan rates.

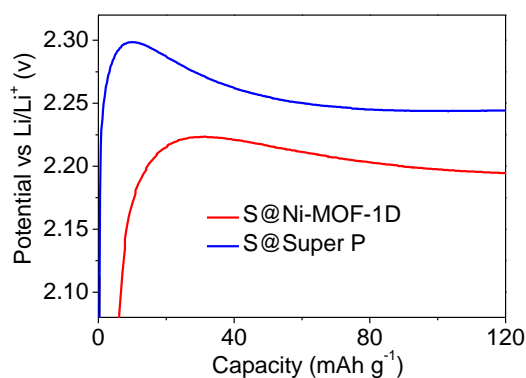


**Figure S21.** Charge profiles of S@Ni-MOF-1D, and S@Super P electrodes showing the overpotentials for conversion between soluble LiPS and insoluble  $Li_2S_2/Li_2S$ .

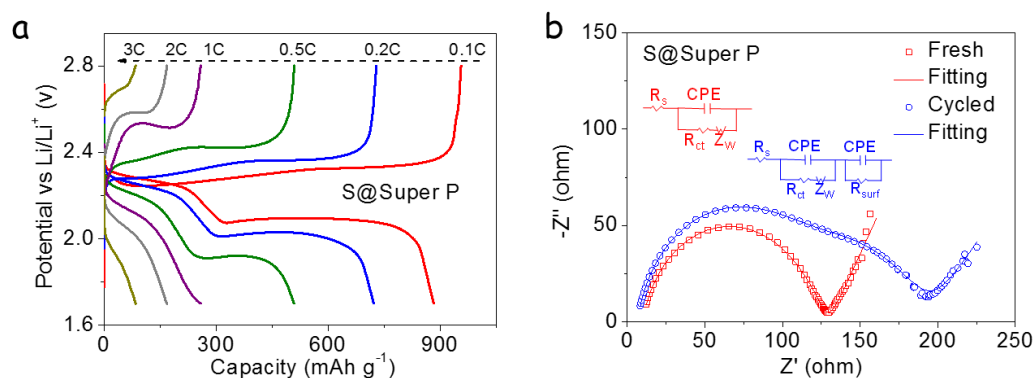


**Figure S22.** (a) Galvanostatic charge/discharge profiles of S@Super P electrodes at different current densities range from 0.1 C to 3 C. (b) EIS spectra of S@Super P coin cells before and after cycling. Blue trace corresponds to fresh cell and red trace to the same cell after cycling. The  $R_s$ ,  $R_{ct}$ ,  $R_{surf}$ , and  $Z_w$  stand for the resistance of the electrolyte, interfacial charge-transportation, insoluble  $\text{Li}_2\text{S}_2/\text{Li}_2\text{S}$  layer, and semi-infinite Warburg diffusion, respectively; and CPE stands for the corresponding capacitance.

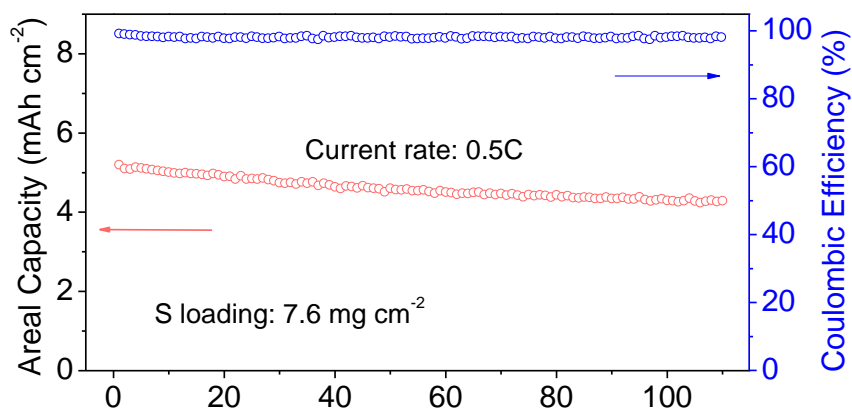


**Figure S23.** High-loading cycling performances with sulfur loadings of  $7.6 \text{ mg cm}^{-2}$  at 0.5 C of S@Ni-MOF-1D electrodes.

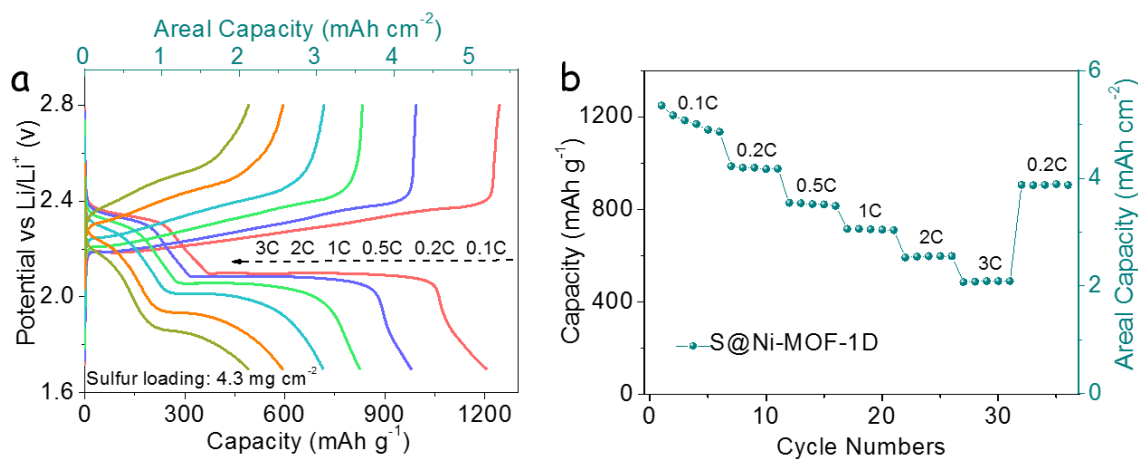


**Figure S24.** (a) Galvanostatic charge/discharge profiles of S@Ni-MOF-1D at various current rates with a high sulfur loading of 4.3 mg cm<sup>-2</sup>. (b) Rate capability of S@Ni-MOF-1D cathodes loaded with 4.3 mg cm<sup>-2</sup> of sulfur at various C rates.

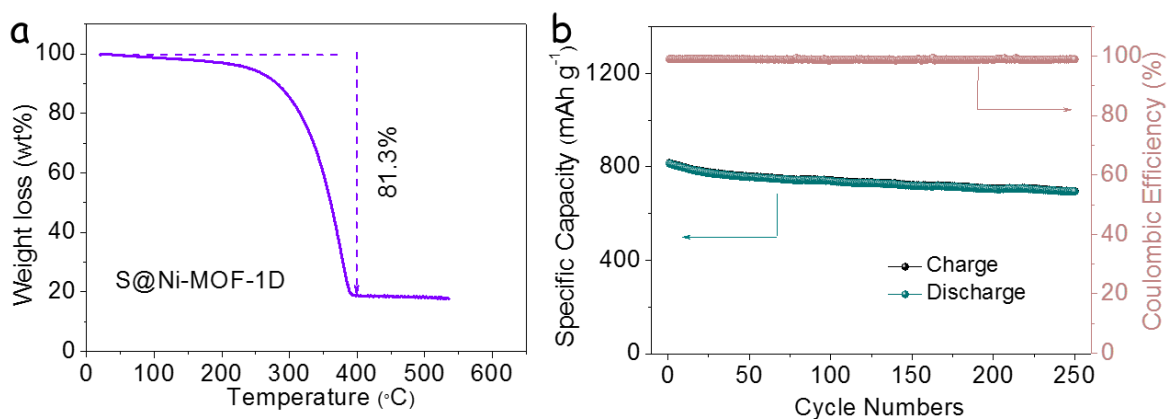


**Figure S25.** (a) TGA curve of a S@Ni-MOF-1D composite with a higher sulfur loading. (b) Cycling stability and Coulombic efficiency of the S@Ni-MOF-1D cathode with a higher sulfur loading at 1 C for 250 cycles.

**Table S2** Summary of recent reports on MOF-based sulfur host cathodes for LSBs.

Host material	Capacity (mAh g <sup>-1</sup> ) (current rate)	(cycles, current rate)	Decay rate (per cycle, %)	S content (%)	Ref
Zr-MOF	1193 (0.1C)	(100, 0.2C)	0.29%	45%	6
DMAZF MOF	1260 (0.1C)	(120, 0.1C)	0.07%	70%	7
Cr-MOF	1190 (0.1C)	(300, 2.4C)	0.07%	41.2%	8
ZIF-8	1150 (0.2C)	(100, 0.1C)	0.085%	64%	9
HKUST-1	1102 (0.2C)	(500, 0.2C)	0.080%	40%	10
Na <sub>2</sub> Fe[Fe(CN) <sub>6</sub> ]	1020 (0.1C)	(100, 0.1C)	0.251%	50%	11
MIL-53	1215 (0.1C)	(300, 0.5C)	0.186%	50%	12
Al/Cu-MOF	974.2 (0.1C)	(200, 0.1C)	0.25%	62%	13
RANEY® nickel	1469 (0.1C)	(500, 0.5C)	0.12%	36.6%	14
Ni <sub>3</sub> (HITP) <sub>2</sub>	1151 (0.2C)	(300, 1C)	0.116%%	65.5%	15
Ni <sub>6</sub> (BTB) <sub>4</sub> (BP) <sub>3</sub>	689 (0.1C)	(100, 0.1C)	0.110%	60%	16
<b>Ni-MOF-1D</b>	<b>1491 (0.1C)</b>	<b>(1000, 3C)</b>	<b>0.018%</b>	<b>70.2%</b>	<b>This work</b>

## References

- [1] G. Kresse, J. Furthmüller, *Phys. Rev. B.* **1996**, *54*, 11169-11186.
- [2] P. E. Blöchl, *Phys. Rev. B.* **1994**, *50*, 17953-17979.
- [3] J. Sun, A. Ruzsinszky, J. P. Perdew, *Phys. Rev. Lett.* **2015**, *115*, 036402.
- [4] J. Sun, R. C. Remsing, Y. Zhang, Z. Sun, A. Ruzsinszky, H. Peng, Z. Yang, A. Paul, U. Waghmare, X. Wu, M. L. Klein, J. P. Perdew, *Nat. Chem.* **2016**, *8*, 831-836.
- [5] Q. Zhang, Y. Wang, Z. W. Seh, Z. Fu, R. Zhang, Y. Cui, *Nano Lett.* **2015**, *15*, 3780-3786.
- [6] A. E. Baumann, X. Han, M. M. Butala, V. S. Thoi, *J. Am. Chem. Soc.* **2019**, *141*, 17891-17899.
- [7] M. Rana, H. A. Al-Fayaad, B. Luo, T. Lin, L. Ran, J. K. Clegg, I. Gentle, R. Knibbe, *Nano Energy* **2020**, *75*, 105009.

- [8] Z. Zhao, S. Wang, R. Liang, Z. Li, Z. Shi, G. Chen, *J. Mater. Chem. A* **2014**, *2*, 13509-13512.
- [9] H. Zhang, W. Zhao, M. Zou, Y. Wang, Y. Chen, L. Xu, H. Wu, A. Cao, *Adv. Energy Mater.* **2018**, *8*, 1800013.
- [10] Y. Mao, G. Li, Y. Guo, Z. Li, C. Liang, X. Peng, Z. Lin, *Nat. Commun.* **2017**, *8*, 14628.
- [11] D. Su, M. Cortie, H. Fan, G. Wang, *Adv. Mater.* **2017**, *29*, 1700587.
- [12] J. Zhou, R. Li, X. Fan, Y. Chen, R. Han, W. Li, J. Zheng, B. Wang, X. Li, *Energy Environ. Sci.* **2014**, *7*, 2715.
- [13] P. Geng, M. Du, X. Guo, H. Pang, Z. Tian, P. Braunstein, Q. Xu, *Energy Environ. Mater.* **2021**, DOI: 10.1002/eem2.12196.
- [14] X. Zhu, J. Tian, X. Liu, W. Huang, D. Luo, Z. Wang, Z. Shan, *RSC Adv.* **2017**, *7*, 35482.
- [15] D. Cai, M. Lu, Li, J. Cao, D. Chen, H. Tu, J. Li, W. Han, *Small* **2019**, *15*, e1902605.
- [16] J. Zheng, J. Tian, D. Wu, M. Gu, W. Xu, C. Wang, F. Gao, M. H. Engelhard, J. G. Zhang, J. Liu, J. Xiao, *Nano letters.* **2014**, *14*, 2345-2352.